Geophysical Journal International

Geophys. J. Int. (2014) **197,** 322–334
Advance Access publication 2014 January 6

doi: 10.1093/gji/ggt505

Magma displacements under insular volcanic fields, applications to eruption forecasting: El Hierro, Canary Islands, 2011–2013

A. García,[1] A. Fernández-Ros,[2] M. Berrocoso,[2] J. M. Marrero,[3] G. Prates,[2,4] S. De la Cruz-Reyna[5] and R. Ortiz[1]

[1] *Geosciences Institute IGEO, CSIC-UCM. J. Gutierrez Abascal, 2, Madrid E-28006, Spain. E-mail: aliciag@mncn.csic.es*
[2] *LAG-Faculty of Sciences, Cádiz University, Puerto Real, Cádiz E-11510, Spain*
[3] *Volcanic Hazard and Risk Consultant, Tenerife, Canary Islands E-38410, Spain*
[4] *Universidade do Algarve, P-8005-139 Faro, Portugal*
[5] *Instituto de Geofísica, Universidad Nacional Autónoma de México, C. Universitaria, México D.F. 04510, México*

Accepted 2013 December 13. Received 2013 December 12; in original form 2013 March 21

SUMMARY

Significant deformations, followed by increased seismicity detected since 2011 July at El Hierro, Canary Islands, Spain, prompted the deployment of additional monitoring equipment. The climax of this unrest was a submarine eruption first detected on 2011 October 10, and located at about 2 km SW of La Restinga, southernmost village of El Hierro Island. The eruption ceased on 2012 March 5, after the volcanic tremor signals persistently weakened through 2012 February. However, the seismic activity did not end with the eruption, as several other seismic crises followed. The seismic episodes presented a characteristic pattern: over a few days the number and magnitude of seismic event increased persistently, culminating in seismic events severe enough to be felt all over the island. Those crises occurred in 2011 November, 2012 June and September, 2012 December to 2013 January and in 2013 March–April. In all cases the seismic unrest was preceded by significant deformations measured on the island's surface that continued during the whole episode. Analysis of the available GPS and seismic data suggests that several magma displacement processes occurred at depth from the beginning of the unrest. The first main magma movement or 'injection' culminated with the 2011 October submarine eruption. A model combining the geometry of the magma injection process and the variations in seismic energy release has allowed successful forecasting of the new-vent opening.

Key words: Volcano seismology; Pluton emplacement; Magma migration and fragmentation; Volcano monitoring; Volcanic hazards and risks; Atlantic Ocean.

1 INTRODUCTION

El Hierro Island (27.7°N; 18.0°W) is the smallest (287.5 km^2) and the youngest (<2 Ma) of the Canary Islands (Ancochea *et al.* 1994; Guillou *et al.* 1996); the maximum altitude in its central sector is 1501 m asl, and it rises from a seafloor almost 4000 m deep (Fig. 1). It has the highest concentration of volcanoes in the Canaries, with more than 500 visible volcanic cones, 300 covered by recent lavas and 70 volcanic caves and galleries. Hernández-Pacheco (1982) states that the last El Hierro eruption occurred in 1793, and Carracedo *et al.* (2001) suggest that it was submarine. Both authors report that some seismic unrest preceded that eruption.

The island's morphology (Fig. 2) has been interpreted as a triple volcanic rift: NE, NW and S rifts (Carracedo 1994), with axes diverging about 120°(Carracedo *et al.* 1999), showing abundant dykes and fissures (Gee *et al.* 2001a), as well as large landslides (Day *et al.* 1997; Masson *et al.* 2002; Mitchell *et al.* 2002). The S-rift submerged axis extends to a distance of 38 km from the coast, with a mean slope of 4° (Gee *et al.* 2001b). The oldest emerged lavas of El Hierro have been found at El Tiñor volcano (NE-rift), and the youngest at Tanganasoga volcano (NW-rift). Three main gravitational landslides have been identified between the three rift alignments: the El Golfo northward landslide separating the NW and NE rifts, the Las Playas eastward landslide between the NE and S rifts and the El Julan southward landslide between the S and NW rifts (Masson *et al.* 2002).

The internal structure of the island shows some interesting features: Bosshard & Macfarlane (1970) place the Moho at 14–15 km under the surface, and Watts (1994) even deeper, at 15–16 km. Carbó *et al.* (2003) made a detailed description of the Canary Islands structure from an extensive gravimetric survey. They report a strong N–S linear gradient (3.5 mGal km^{-1}) from La Palma and extending across El Hierro. The existence of an intrusive body displaced northeastwards away from the El Hierro NE-rift, which

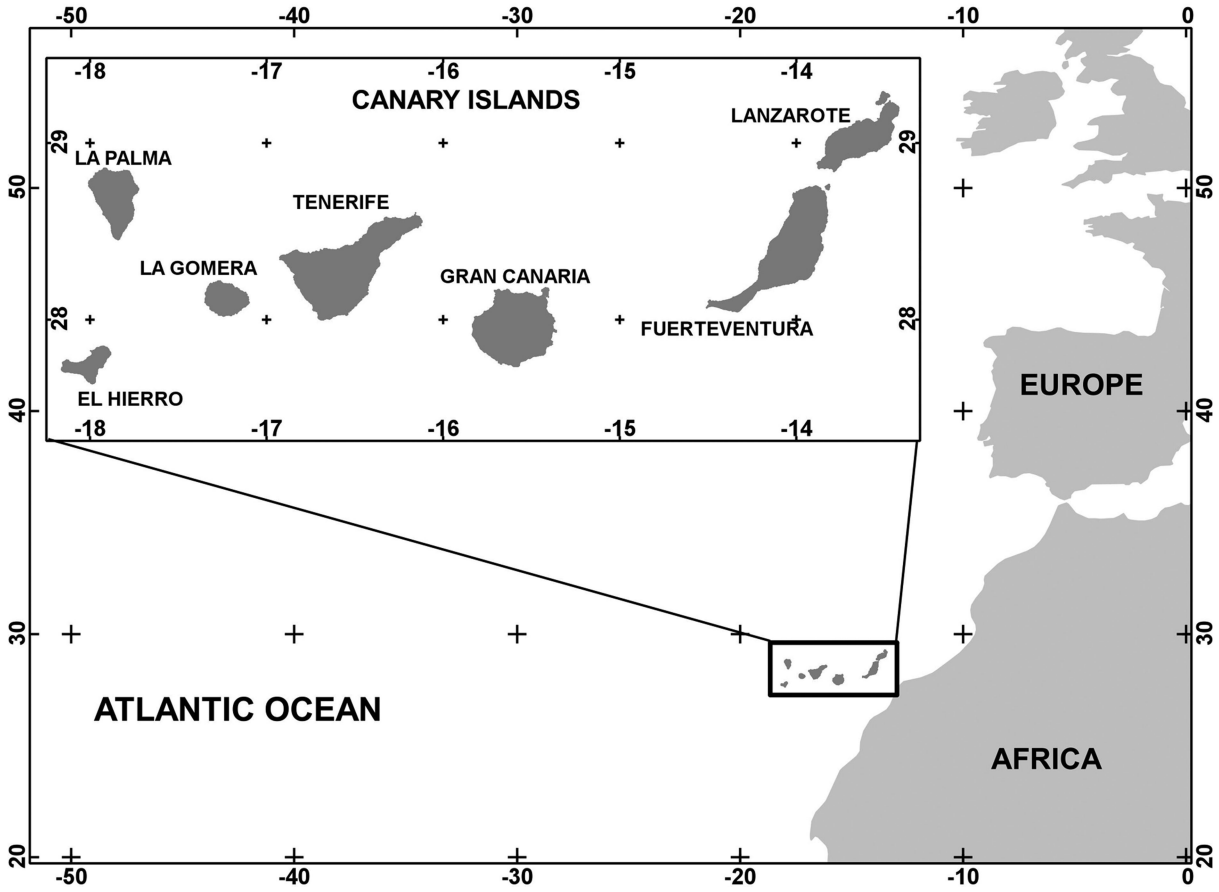

Figure 1. Location of El Hierro and the Canary Islands.

might be associated with the last island formation phase, has been inferred from gravity data by Montesinos *et al.* (2005, 2006). However, Catalán & Martín Davila (2003) did not find geomagnetic evidence of magma beneath El Hierro. A more recent aeromagnetic survey provided data for a more detailed model of the rift zones and internal structure of El Hierro Island (Blanco-Montenegro *et al.* 2008). In addition, recent microseismic soundings revealed two intrusive bodies extending downwards from 10 km to at least 30 km in depth (Gorbatikov *et al.* 2010). One body underlies the El Tiñor edifice, associated with the island's earlier formation stages (1.2–0.88 Myr; Carracedo *et al.* 2012), while the other is located on the NW-rift western edge, associated with a younger stage (<158 Ky; Carracedo *et al.* 2012). According to Stroncik *et al.* (2009), the volcanic activity at El Hierro is controlled by a complex array of small, isolated magma pockets at mantle depths. Such a mechanism favours low melt production rates, which seems to be a characteristic of ocean islands not fed by central conduit systems, as is the case of intraplate plume-fed systems. The depths of such small magma batches range between 12 and 30 km, and they may be interconnected by complex arrays of sills or dykes where discrete magma batches have mixed over different timescales, making magma ascent from those depths possible without it having been previously stored in the crust.

In 2011 July, a significant increase of seismic activity was detected at El Hierro Island. This prompted various Spanish institutions to deploy a variety of instruments to monitor the activity: the National Geographic Institute (IGN; López *et al.* 2012); the Canaries Volcanology Institute (INVOLCAN; Pérez *et al.* 2012); the University of Cádiz (UCA; Prates *et al.* 2013b) and the Spanish National Research Council (CSIC). In particular, the CSIC–UCA team members have been analysing seismic and GPS deformation data in real time, aiming to follow up the evolution of the volcanic crisis, and to forecast its outcomes. Fig. 3 shows the distribution of seismic and GNSS-GPS networks. At the beginning of the unrest, only one public GNSS-GPS permanent station (FRON) operated by GRAFCAN (Government of Canaries) and located in the Frontera municipality was available on the island. Other permanent public stations located on other Canary Islands (Fig. 3) have also provided useful reference information. Real-time geodynamic control of the LPAL station is carried out using the MAS1 and RBAT (Morocco) stations (Prates *et al.* 2013b).

As stated, the seismic activity at El Hierro persistently increased since 2011 July. This trend changed in 2011 September, when the level of seismic activity showed an accelerating tendency preceding a submarine eruption (27°37.18′N; 17°59.58′W), first detected on 2011 October 10, and lasting until 2012 February (López *et al.* 2012). From the analysis of the seismic activity, and particularly the hypocentre locations, two distinct stages preceding the eruption could be recognized: from July 19 until 2011 September 3, the hypocentres were clustered under El Golfo valley and the Tanganasoga volcano at depths of 15–20 km. After 2011 September 4, the hypocentres migrated southwards until the onset of the eruption on October 10. The eruption was first recognized by the detection of a strong tremor signal, immediately followed by sea surface manifestations such as steam emissions, strong greenish coloration of the ocean water and the appearance of floating pumice-like blocks (Carracedo *et al.* 2012; López *et al.* 2012).

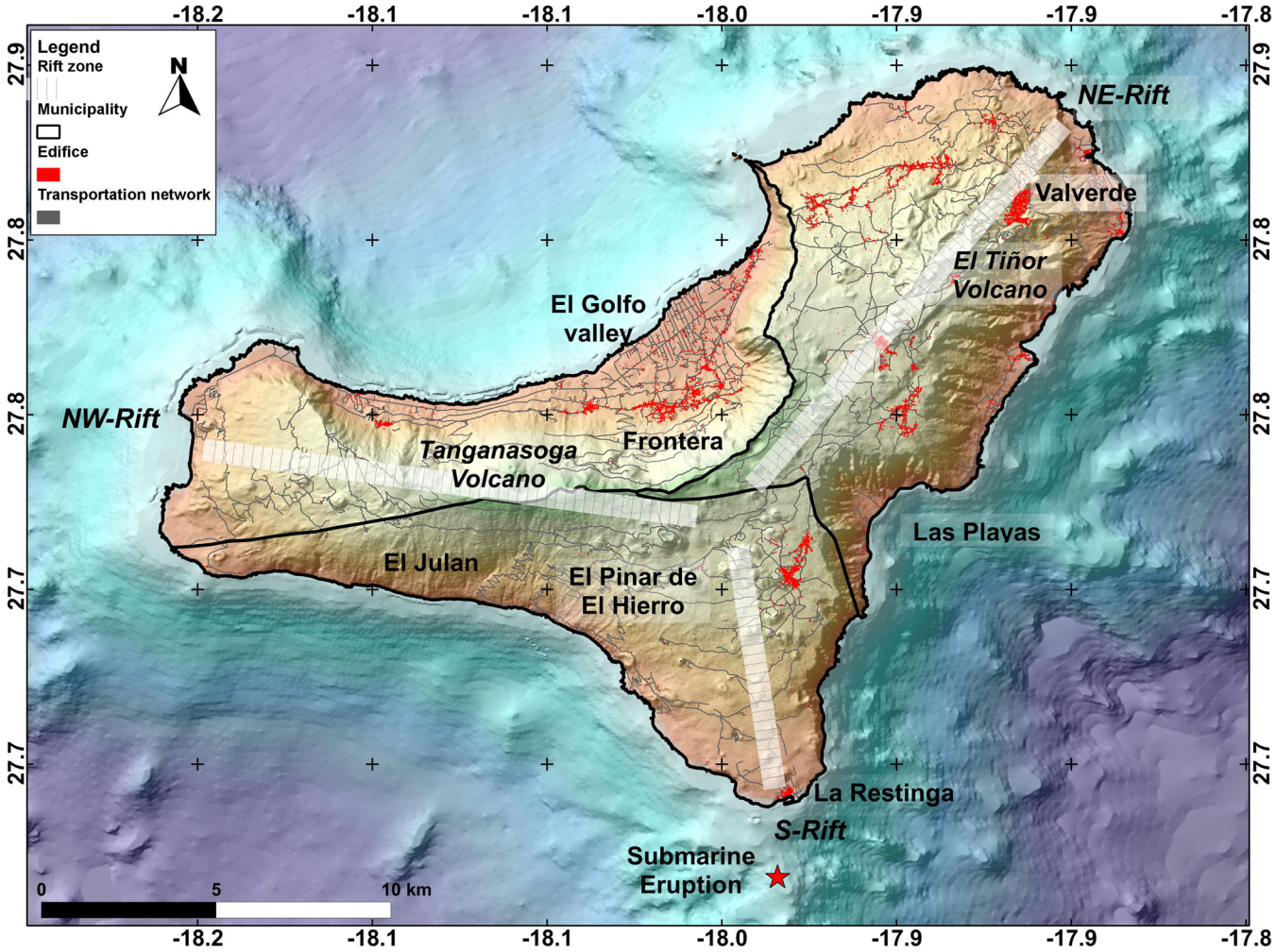

Figure 2. Morphology and main structural features [triple volcanic rift: NE, NW and S, according to Carracedo (1994)] of El Hierro Island. The locations of the municipalities (Valverde, El Pinar de El Hierro and Frontera), the town of La Restinga and the submarine eruption site are also shown.

Seismic activity resumed on 2011 October 20 in the northern sector of the island. The strongest earthquakes, many of them felt throughout the island, occurred before (23 September 23 to October 8) and after the onset of the eruption (November 2–11). A detailed discussion on this seismicity may be found in Ibáñez *et al.* (2012). After analysing the seismic catalogue (http://www.ign.es), those authors reported an anomalous lack of shallow seismicity, and a variable rate of seismicity. During the following months, the seismic activity continued, including earthquakes exceeding M 3.5, particularly in 2012 June–July, September and December, 2013 January and 2013 March–April. We assume that each of those high seismic activity episodes is related to magma displacements at depth, from which at least a single eruption resulted. According to Gudmundsson (2000, 2002), Gudmundsson & Brenner (2001, 2004) and De la Cruz-Reyna & Yokoyama (2011), dykes and inclined sheets injected from magma reservoirs frequently fail to reach the surface to feed volcanic eruptions, thus making many of the magma-induced seismic swarms 'failed eruptions'.

Here, we present the results of the analysis of seismic and GNSS-GPS data processed in quasi-real time as the volcanic crisis developed during the period 2011 July to 2013 July and submitted to the crisis managers attempting to provide useful decision-making factors. Among these factors were: expected trend of incoming seismicity, assessment of the possibilities of higher magnitude earthquakes, land-slides and forecasting of time and place of volcanic eruptions. The theoretical framework for such assessments and forecastings was based on the combination of a Mogi-based deformation model (Mogi 1958; McTigue 1987; Lisowski 2006), a maximum-differential stress model resulting from the combination of a point-pressure source and the lithostatic load (Sezawa 1931; McTigue 1987; De la Cruz-Reyna & Yokoyama 2011), and an empirical magma injection-seismic energy model of Yokoyama (1988). This combination proved effective to forecast most of the significant events along the duration of the crisis.

2 SEISMIC ENERGY AND MAGMA INJECTION MODELS

Yokoyama (1988) proposed an empirical relationship for a threshold of cumulative seismic energy released preceding magmatic eruptions in closed volcanic systems, after long periods of repose. He concluded that eruptions may occur when the cumulative seismic energy released during the precursory stage reaches a threshold cumulative energy of about 10^{11} J $\pm$ one order of magnitude. This threshold energy may be related to the volume of rock fractured by the magma that will erupt, and may be valid for central andesitic volcanoes and for monogenetic volcanoes

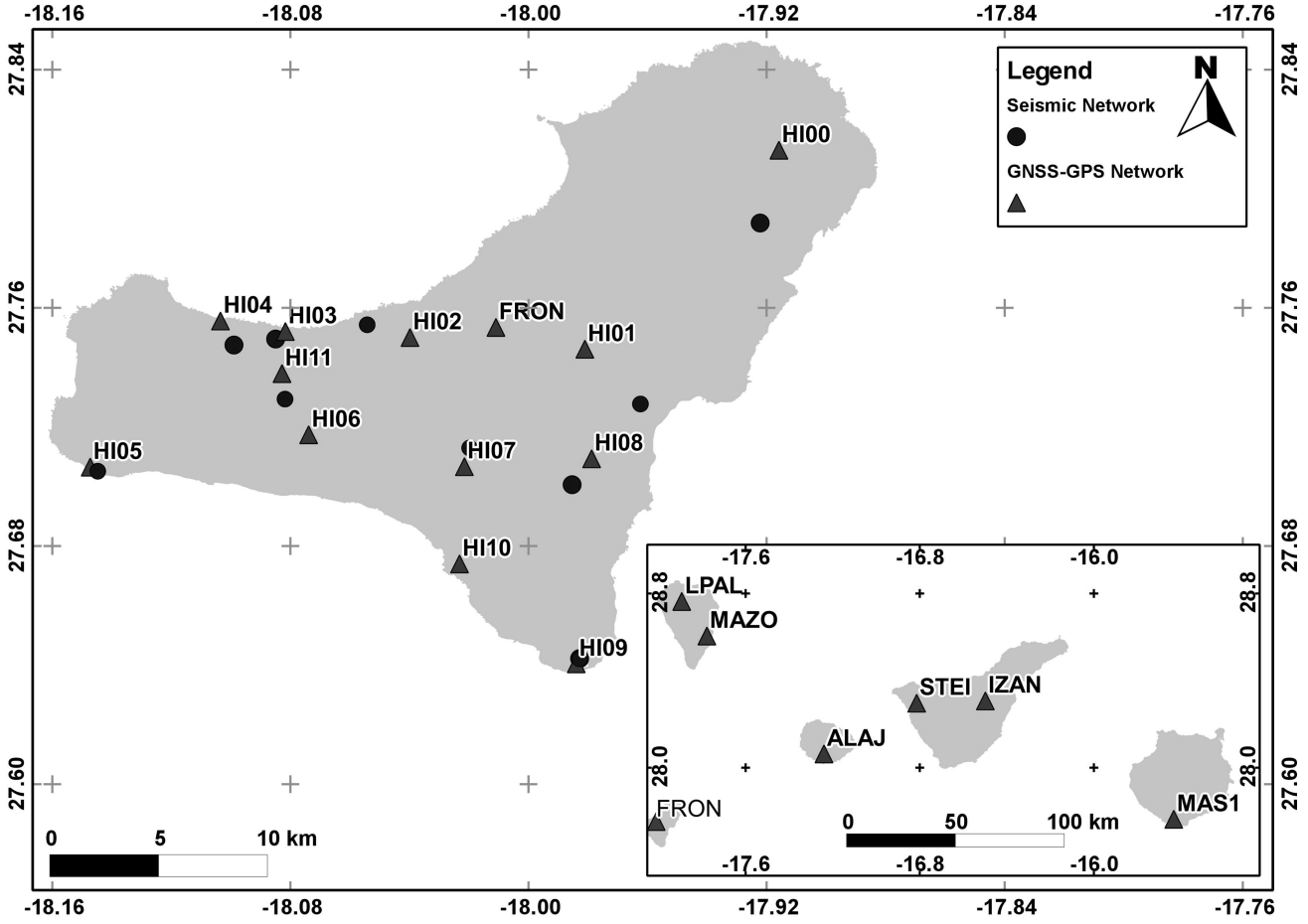

Figure 3. Location of seismic and GNSS-GPS stations (IGN, UCA and CSIC networks). LPAL belongs to the IGS network and it was therefore selected as a reference station for the GNSS-GPS data processing for the entire seismic crisis and eruptive process. ALAJ, MAZO, IZA and STEI have been used as control stations.

(De la Cruz-Reyna & Yokoyama 2011). In addition, the cumulative seismic energy evolution shows a behaviour similar to the evolution of the observables of the volcano activity proposed by Voight (1988; Failure Forecast Method, FFM). The FFM has frequently been applied to forecast the event time in volcano monitoring (Voight & Cornelius 1991; De la Cruz-Reyna & Reyes-Dávila 2001; Ortiz *et al.* 2003; Tárraga *et al.* 2008). There are diverse interpretations and implementations for its application to the forecasting of the volcanic phenomena (Kilburn 2003, 2012; De la Cruz-Reyna *et al.* 2008; Bell *et al.* 2011), depending on the observable used and on the calculation procedure. Magma induces additional stresses on the confining country rock in which it is intruding. When the combination of this stress with the regional tectonic stress reaches a critical value, the induced fracturing, or reactivation of pre-existent fractures, allows magma, and magma-related fluids to find their paths to the surface (Voight & Cornelius 1991; De la Cruz-Reyna & Yokoyama 2011). Assuming a simple model consisting of a small spherical pressure source of radius a, at a depth D below the horizontal surface of a solid half-space, solutions of the surface deformation when the pressure P_0 in the sphere exceeds the lithostatic pressure were first found by Sezawa (1931) for a general plastic medium. Later, Mogi (1958) used those results to compare that model with field data of volcanic deformations. A simplified solution based on the assumption $a/D \ll 1$ (point dilatation) includes the quantity a^3P_0, known as the intensity of the singularity, since the stresses at the point dilatation are singular (McTigue 1987). The medium thus undergoes a maximum horizontal differential stress at the radial distance $r = \pm 0.82D$, corresponding to a dip angle (ϕ) between the pressure source and the site of potential fracturing near the surface of 51°. This model thus considers that, in a homogeneous elastic medium, the maximum differential stress defines an inverted cone with its apex at a depth D, at the point dilatation and its base on the crustal surface as a circle with radius $0.82D$.

We adopt this conceptually simple model considering that our analysis is focused on the time and space evolution of the magma-induced pressure sources, and not on the precise determination of their pressures, locations and dimensions. The validity and possible limitations of the model and their consequences on our results are discussed in the final section of this paper.

3 EL HIERRO PROCESS: SEISMICITY AND DEFORMATION

The unrest episode at El Hierro occurred after a long repose period (over 200 yr). According to the empirical model of Yokoyama (1988), an eruption may occur in a closed volcanic system if the volcano-tectonic (VT) seismic energy exceeds a threshold of the order of 10^{11} J. Accordingly, using cumulative VT energy from the earliest stages of the unrest may be a more reliable parameter, as it is controlled by the largest magnitude events, unlike the statistics of the number of events, controlled by the smallest, more frequent, events.

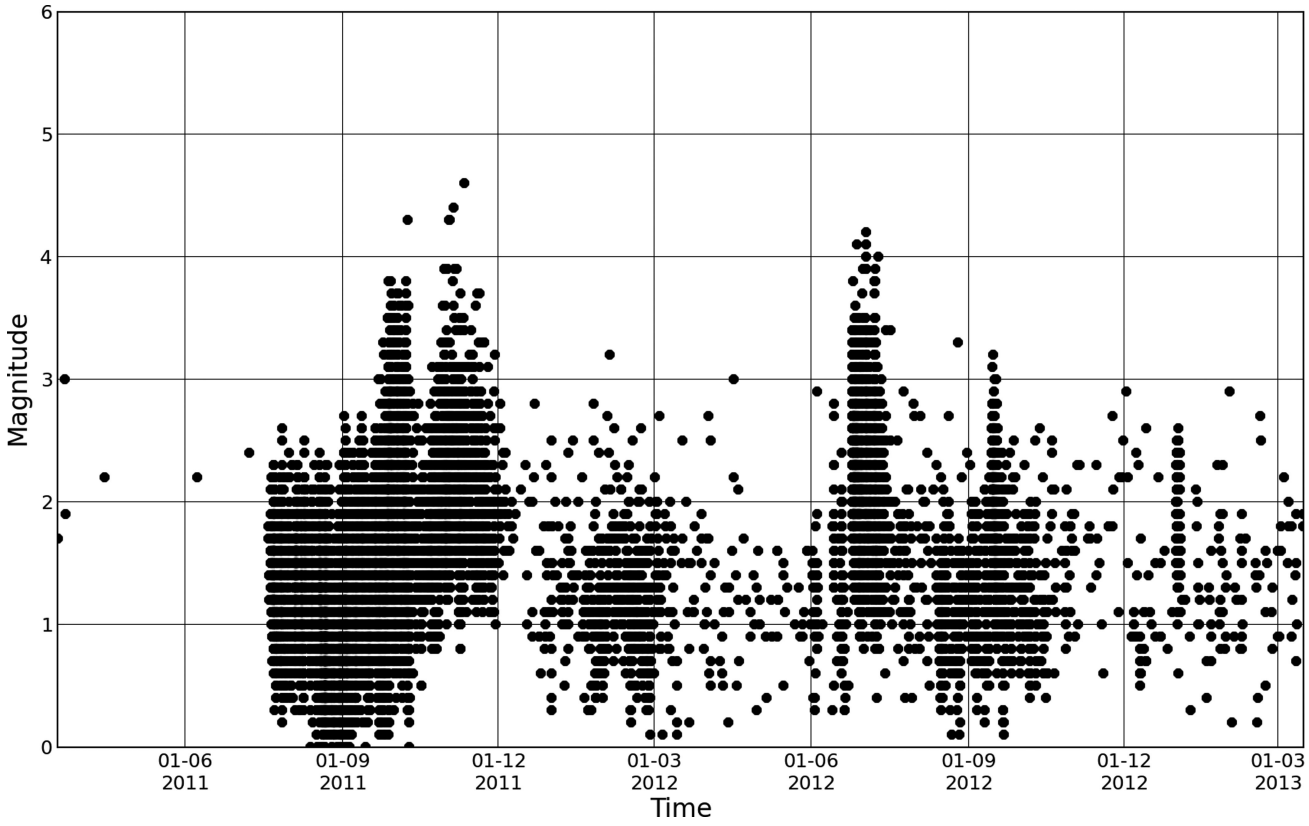

Figure 4. Time evolution of the volcano-tectonic earthquake magnitudes. The peculiar behaviour of the low-magnitude cut-off seemingly correlated with the appearance of higher magnitude VT events may be an artefact of the official catalogue reporting method, as only a limited number of events may be sensibly included.

In a small island, as is the case of El Hierro, localization of earthquakes outside the area of the seismic network may be affected by large errors (Ibáñez *et al.* 2012). Small earthquake ($M < 2$) location may be unreliable due to the oceanic and anthropogenic noise, a problem that becomes particularly serious in the initial phase of the unrest, when the dominant activity is small earthquakes. In the El Hierro crisis, significant increases of earthquake magnitude have been observed around 10 d or less before an eruption. Fig. 4 shows the time evolution of the earthquake magnitudes from the beginning of the unrest until 2013 July.

Fig. 5 shows how the cumulative seismic energy grew until it reached a level of 10^{11} J on 2011 September 23. From then on, the magnitude of earthquakes rose rapidly, exceeding magnitude 4 on 2011 October 8. 2 d later, on 2011 October 10, all seismic stations recorded a high-amplitude tremor which signalled the onset of a submarine eruption from a vent located about one nautical mile from the southernmost coast of the island, facing the town of La Restinga. After the opening of the emission centre, the VT activity temporarily decayed. However, this activity restarted on 2011 October 15, showing again an increasing trend of the cumulative seismic energy, until it again reached 10^{11} J on 2011 October 29. From that date on, the seismicity patterns changed again, and the proportion of higher magnitude earthquakes increased, some exceeding M 4. On 2011 November 2, the tremor signal amplitude increased again in all of the seismic network stations, lasting for several days. On 2011 November 11, an M 4.6 earthquake was recorded and magnitudes subsequently decreased. A new process began in 2012 June–July, culminating with earthquakes exceeding M 4. This process was similar to the previous ones, the main difference being the shorter duration of the accelerated seismicity stage that probably resulted from a change of the initial conditions of the system in this new episode. The 2013 March–April process was also similar but the cumulative seismic energy reached 108.6×10^{11} J, much greater than in the preceding processes (12.7, 18.6 and 19.8×10^{11} J). In this last process the largest earthquake reached magnitude 4.9 (2013 March 31; Fig. 5 and Table 1). It seems that in this type of process also the seismic risk increases significantly when the cumulative VT energy approaches 10^{11} J, since in such a situation most of the energy tends to be released by larger magnitude earthquakes (approaching 5.0), capable of damaging buildings and triggering landslides. In all plots of Fig. 5 the cumulative seismic energy has been reset to zero at the end of each episode, when most of the magnitudes did not exceed magnitude 2 (see Fig. 4).

The available GNSS-GPS data were specifically processed in quasi-real time for early detection of new pressure sources and evolution of the volcanic activity. The steps followed for the GNSS-GPS data processing are:

(1) BERNESE GPS Software 5.0 Process (Dach *et al.* 2007).
(2) Determination of accurate absolute positions (X, Y, Z, t) in quasi-real time.
(3) Topocentric coordinates (e, n, h).
(4) Kalman filtering of time-series (Kalman 1960).
(5) Calculation of displacements velocities for each benchmark (Dzurisin 2006).
(6) Calculation of Mogi source parameters (latitude, longitude, depth and volume change; Mogi 1958; McTigue 1987; Lisowski 2006) using the simulated annealing model inversion (Press *et al.* 2007).

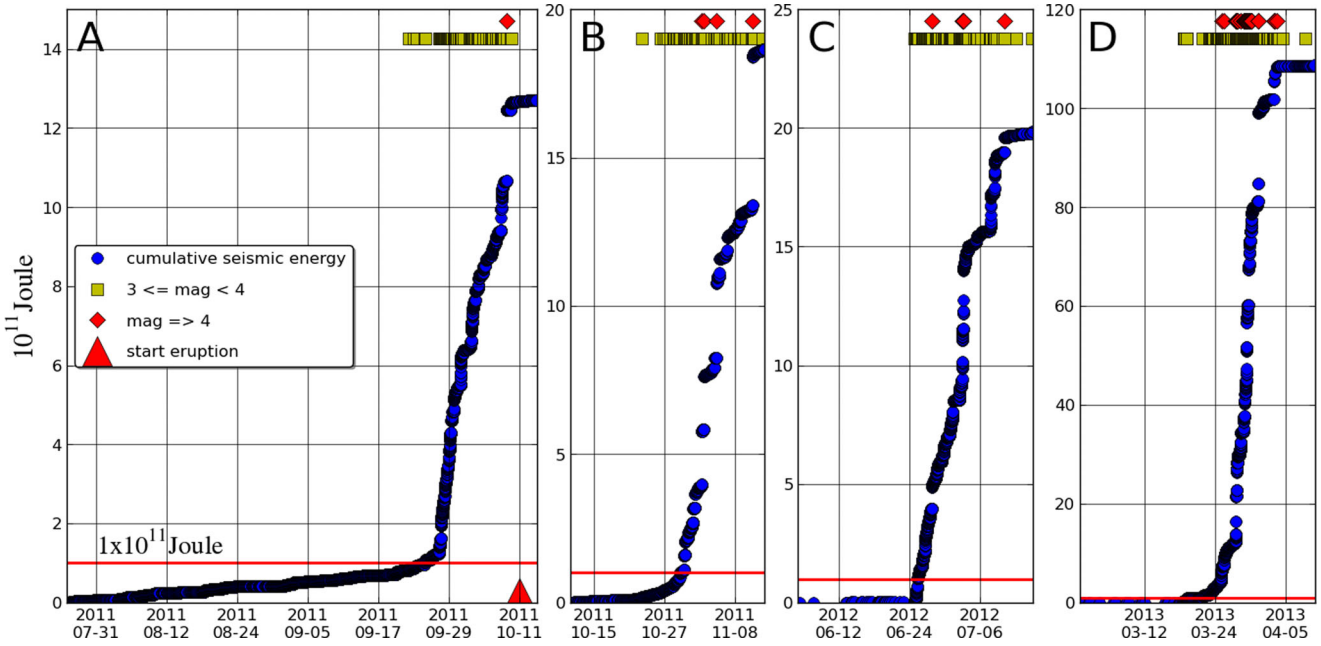

Figure 5. Evolution of the cumulative seismic energy for the repetitive episodes of seismicity associated to magma migration processes: (A) from the beginning of the unrest until the onset of the eruption; (B) second unrest episode which reached its climax on 2011 November 11 with an earthquake of *M* 4.6 earthquake; (C) seismic unrest episode of 2012 June–July; (D) seismic unrest episode of 2013 March–April including an *M* 4.9 earthquake and several landslides.

Table 1. Earthquakes of magnitude 4 or higher (from the IGN official catalogue) recorded during the seismic crises episodes identified in Fig. 5.

Date	Mag	Date	Mag	Date	Mag
Episode A		Episode B		Episode C	
2011-10-08 20:34:48	4.3	2011-11-02 07:54:55	4.3	2012-06-27 18:55:08	4.1
		2011-11-02 18:10:39	4.3	2012-07-02 22:42:38	4.1
		2011-11-04 20:36:28	4.4	2012-07-03 02:26:51	4.0
		2011-11-11 00:20:16	4.6	2012-07-03 02:31:02	4.2
				2012-07-10 04:04:34	4.0
Episode D					
2013-03-25 05:57:21	4.0	2013-03-29 03:15:17	4.2	2013-03-29 19:56:00	4.0
2013-03-25 14:41:39	4.1	2013-03-29 05:15:08	4.0	2013-03-30 00:30:35	4.3
2013-03-27 15:02:15	4.4	2013-03-29 07:58:04	4.1	2013-03-30 04:12:25	4.1
2013-03-27 15:07:56	4.6	2013-03-29 08:13:52	4.0	2013-03-30 04:33:34	4.0
2013-03-27 15:28:56	4.2	2013-03-29 08:14:44	4.5	2013-03-30 05:04:18	4.2
2013-03-27 16:10:54	4.5	2013-03-29 09:41:48	4.6	2013-03-31 09:40:46	4.5
2013-03-27 17:54:29	4.2	2013-03-29 10:11:06	4.1	2013-03-31 10:59:54	4.9
2013-03-27 19:55:31	4.2	2013-03-29 12:42:58	4.0	2013-04-03 02:45:26	4.5
2013-03-28 11:00:16	4.3	2013-03-29 17:01:21	4.7	2013-04-03 03:41:26	4.2
2013-03-28 22:22:47	4.2	2013-03-29 19:30:22	4.3	2013-04-03 11:16:12	4.2
2013-03-29 02:51:33	4.4	2013-03-29 19:52:18	4.1		

Steps 1–3 are usual in the GNSS-GPS data processing. In step 4 subdaily solutions enhanced with Kalman filtering (Kalman 1960; Berrocoso *et al.* 2012; Prates *et al.* 2013a,b) were used to monitor trend shifts in near real time. Steps 5 and 6, are necessary to transform the deformation data into parameters associated with a pressure source that can be used to forecast the evolution of the seismo-volcanic activity. These solutions allowed for a near real-time Mogi pressure source interpretation (Mogi 1958; Lisowski 2006) as the trend shifts occurred. Daily solutions were also obtained, which allowed determining daily Mogi pressure source parameters (Mogi 1958; McTigue 1987). This procedure, combined with the model proposed by Yokoyama (1988), allowed a continuous surveillance of the evolution of the magma injection processes during the El Hierro crisis.

Fig. 6 shows the time variation of the LPAL-FRON distance for the 2011 April–December period, in which two deformation phases are clearly defined. The first phase corresponds to the beginning of the unrest with the seismic activity concentrated in the north of the island. The second phase started in early 2011 September coinciding with a southward faster migration of the seismic activity that ended with the onset of the submarine eruption. In the Kalman-filtered signal (B in Fig. 6) strong short-period (a few hours or days) deformation oscillations could be observed, correlated with the occurrence of seismic events of greater magnitude (e.g. the earthquake of 4.3 on 2011 October 8; Prates *et al.* 2013b). Table 2 presents the inferred geometric source data.

Fig. 7 depicts the application of the De la Cruz-Reyna & Yokoyama (2011) model, and the observed migrations

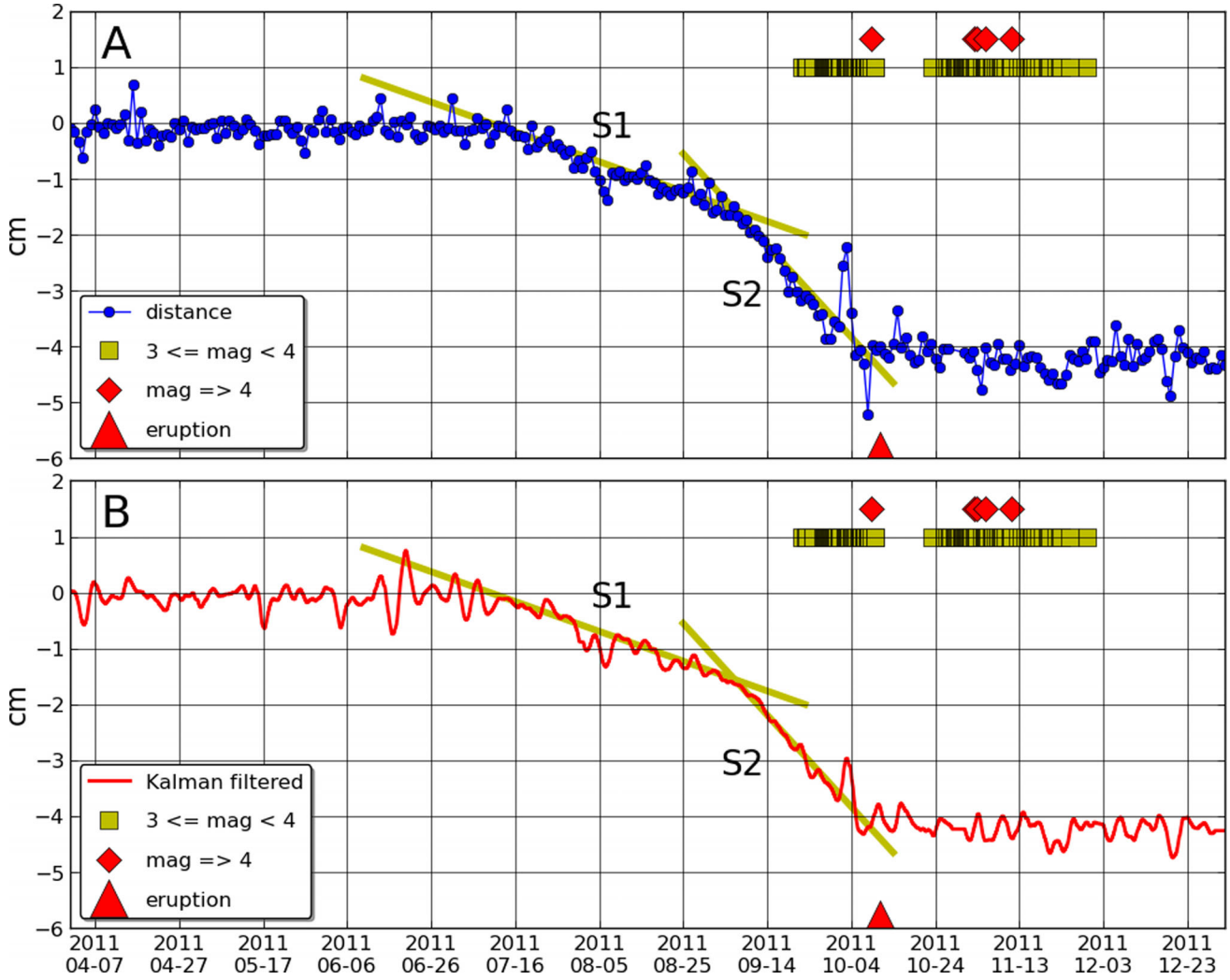

Figure 6. (A) Daily solutions and (B) subdaily Kalman solutions, for LPAL-FRON baseline length for the period 2011 April–December. Two different regimes can be identified by their deformation rates: (S1) onset of unrest and (S2) increased deformation rate.

Table 2. Dates, positions, depths and pressure centre radius/depth ratios for the Mogi Models calculated from the available GPS data.

Date	Latitude	Longitude	Depth (km)	Radius/depth
2011-08-22	27.721	−18.067	17.0	0.030
2011-10-10	27.647	−18.068	7.50	0.057
2011-11-10	27.721	−18.067	17.10	0.021
2012-07-08	27.636	−18.106	13.23	0.071
2012-09-20	27.689	−18.015	8.50	0.077
2013-01-04	27.810	−18.005	7.50	0.074
2013-03-25	27.733	−18.180	11.15	0.073
2013-04-01	27.716	−18.229	12.35	0.079

of seismic foci and evolution of the deformations, to describe the process of magma displacements or injections that culminated with the eruption of 2011 October. From the earliest stages of the unrest, the observed deformations (S1 in Fig. 6) allowed an initial pressure centre M1 to be defined. The injection cone defined by this centre should, according to the model, have a vertical semi-aperture of $90^\circ - 51^\circ = 39^\circ$, generating the circle shown in the upper left part of Fig. 9, as explained later. Starting in 2011 August, the pressure centre, and thus the seismicity migrated in a direction parallel to the south rift (F1). R1 is the generatrix that defines circular sections parallel to the crustal surface. One of those sections, at depth D2 in Fig. 7 includes the pressure source M2, where the magma migrated. We conclude that this is the point where a second pressure source may explain the succeeding deformation stage (S2 in Fig. 6). From then on, this pressure source M2 defined a new injection cone with generatrix R2. Magma would then be displaced preferentially through a path defined by a pre-existing E–W trending fracture F2. The submarine eruption began in 2011 October at the point *e*. The initial pressure source M1 is 17 km deep, beneath the young stratovolcano Tanganasoga, suggesting that this is a relatively weak region, where deeper magma injections may be more likely. The secondary pressure source M2 is 7.5 km deep. These results are compatible with the magma reservoirs proposed by Martí *et al.* (2013), who assume an aseismic ascent of magma from a depth of about 25 km through a channel defined by a major structural discontinuity, to a new magmatic reservoir about 10–12 km deep, and it is also consistent with the InSAR data inversion model source depths of González *et al.* (2013), between 9.5 ± 4.0 and 4.5 ± 2.0 km. The magma paths are thus probably controlled by the maximum differential stress zones acting on pre-existing fractures and zones of weakness. There is however a rather unusual lack of shallow seismicity (<10 km; Ibáñez *et al.* 2012), which may be attributed, as hinted by the reported location errors of the seismic catalogue,

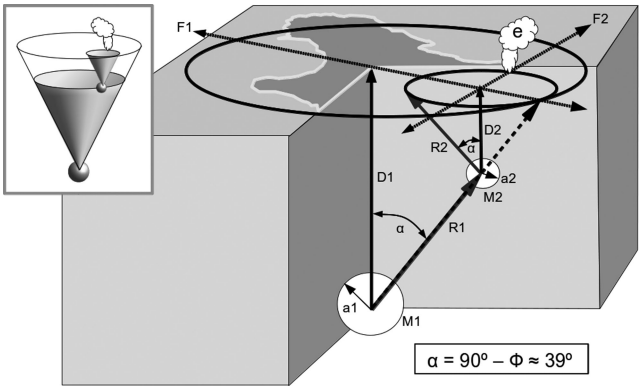

Figure 7. Application of the model of De la Cruz-Reyna and Yokoyama (2011) to the magma injection process that ended with the 2011 October eruption at El Hierro. From an initial pressure centre (M1) the magma preferentially migrates through a path defined by the N–S trending fracture F1. In the intersection of the fractures marked F1 and F2, the accumulated magma forms a second pressure source (M2). From M2, the magma migrates through a new path (F2), reaching the surface at point *e*, starting an eruption. The inset shows an schematic view of the resulting maximum differential stress cones.

to a combination of the geometry of the seismic network with an inadequate seismic velocity model for that region.

Fig. 8 shows in detail the magma migrations from 2011 August to the onset of the eruption. The episode began as a consequence of the emplacement of the initial main pressure centre (2011-08-22, 27.721°N, 18.067°W, 17 km deep), that acted as a 'departure point' for the succeeding magma displacements, as revealed by the spatial distribution of earthquakes with $M > 3.5$. Such distribution reveals a southward path, parallel to the structural N–S axis, from the initial pressure centre. Such southward injection formed a new pressure centre at (2011-10-10, 27.647°N, 18.068°W, 7.50 km), as calculated from the GNSS-GPS data. Then, from that second pressure centre, the seismicity migrated towards the south–east, aiming to the site of the eruption, which is located between the maximum differential stress surface circles of the two initial sources, and near their tangential point, quite consistently with the proposed injection model. The dashed line on the map to the right-hand side of Fig. 8 tracks the path of the $M \geq 3.5$ earthquakes towards the eruptive vent, thus defining an injection path.

As mentioned above, a few days after the onset of the submarine eruption, the spatial distribution of seismicity, and the deformation evolution indicated that a new process of magmatic injection was occurring. This new process started from the first pressure source and moved northwards. Fig. 9 shows the main processes of magma injection occurred between 2011 August and 2013 April. It is important to emphasize that the circular regions were defined from Mogi source models, and calculated each time that the deformation velocity vectors changed. For the seismicity, periods of 20 d prior to the occurrence of the higher magnitude earthquakes optimally show the evolution of seismicity rate changes, as illustrated in Fig. 5. We are thus assuming that the injection episodes are linked, and the 2011 August episode represents the first link of the chain.

We consider very significant that most of the epicentres in each episode are located within the conical cross-section circle defined by the corresponding injection cone on the crustal surface (Fig. 9 and Table 3). However, in 2012 September, a group of earthquakes occurred clearly outside the corresponding circle. Such earthquakes were detected mostly during the first 10 d of the time window. We thus believe that the lack of GPS data at the western end of the island at that time has hindered the definition of other pressure centres for the events beyond the circle. A second similar case, in 2013 March, may have been caused by the concurrent effect of several sources. The seismic activity and locations of the pressure sources on 2013 March 25 and 2013 April 1 is depicted on the right-hand side of Fig. 10.

Fig. 10 also illustrates the seismicity caused by the migration of magma pressure sources in 2012 June–July and

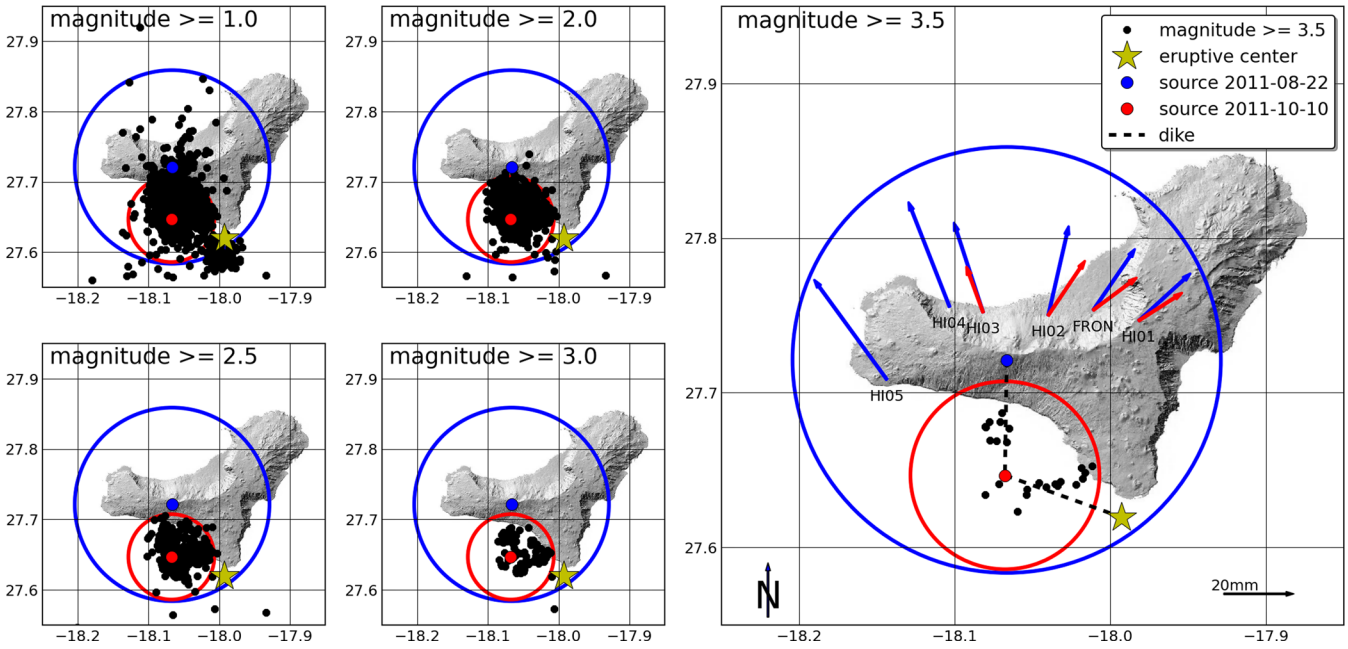

Figure 8. Seismicity for different cut-off magnitudes in the 2011 October unrest episode, and the intersection of the maximum differential stress cones of Fig. 7 with the crustal surface. The arrows represent the horizontal deformation vectors corresponding to the two pressure sources.

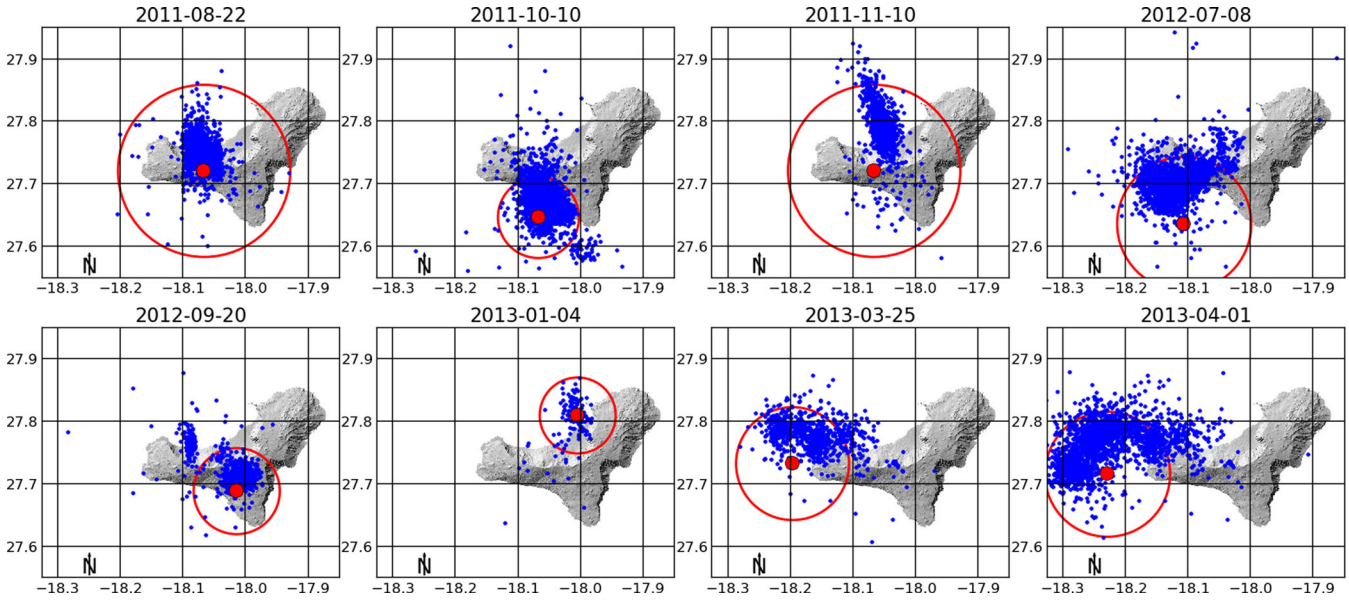

Figure 9. Intersections of the maximum differential stress cones with the island's surface, and seismicity of each of the unrest episodes. Dates, positions, depths and pressure centre radius/depth ratios of the cones generating those circles are listed in Table 2. The smaller circles (2011-10-10, 2012-09-20 and 2013-01-04) correspond to shallower (less than 10 km) secondary pressure sources.

Table 3. Number of seismic events located inside and outside the injection circle of each episode.

Date	Inside	Outside
2011-08-22	2741	8
2011-10-10	2337	447
2011-11-10	1216	48
2012-07-08	1775	271
2012-09-20	549	175
2013-01-04	123	16
2013-03-25	667	180
2013-04-01	1691	403

2013 March–April. In the first period, the seismicity took place within the extent of the seismic network, thus allowing a better determination of the earthquake depths. Shallow earthquakes are bunched close to the circumference defined by the intersection of the cone of maximum horizontal differential stress with the island's surface. In other episodes the inability to detect and locate shallow events (Ibáñez *et al.* 2012) concealed this effect. The strongest seismic activity, the largest magnitude earthquake and the largest number of landslides and shallow earthquakes, all occurred in 2013 March–April.

4 DISCUSSION AND CONCLUSIONS

There is an ample bibliography on the forecasting and emergency management in volcanoes with frequent or persistent activity (e.g. St Helens, Pinatubo, Stromboli, Etna, Piton de La Fournaise). However, little has been published on how to deal with the unrest in an island showing monogenetic volcanism with large return periods. A major difficulty is the '*a priori*' definition of a zone where a new volcanic vent is expected to open, even in the case when geological information on structures that are likely to fail is available, as the differences in eruption likelihood between such zones and the rest of the island may not be significant. In fact, recent volcanic cones are scattered all over the El Hierro island. Notwithstanding, being a small island, it has not aroused sufficient interest in the scientific community, and no detailed crustal models are available to fit the observed seismic and deformation data. However, as a consequence of the unrest and eruption, new research is being published that should allow the application of more complex models to the monitoring efforts of future episodes of unrest.

The recent seismic and volcanic unrest at El Hierro Island has been analysed using the available seismic and GNSS-GPS data, aiming to model the magma displacement processes that precede an eruption. Forecasting the evolution of the activity was done in quasi-real time (with a lapse of less than 24 hr), using models previously proposed by Yokoyama (1988) for the threshold of the cumulative seismic energy, and by De la Cruz-Reyna & Yokoyama (2011) for the determination of regions of maximum differential stress, based on pressure-source models (Mogi 1958; McTigue 1987; Lisowski 2006) inferred from the GNSS-GPS deformation data. Kalman filtering (Kalman 1960) allowed rapid definition (within hours) of the geodetic station displacements and their corresponding pressure centres (Prates *et al.* 2013a,b). The spatial distribution of seismicity has shown a good correlation with the geometry of the magma injection models for the pressure centres inferred from the GNSS-GPS deformation data, despite some seismic location difficulties. The injection model predicts that the seismicity should be distributed along the circumference of a circle defined by the cross-section of the maximum differential stress cone with a horizontal plane at any depth above the pressure centre. This has been observed during the episodes of 2012 June–July and 2013 March–April, when the seismic and landslide activity was mostly located within the area covered by the seismic network, and at a time when the network had the largest number and the best distribution of seismic stations (Fig. 10). The earthquake location errors, and particularly of their depths for the other episodes prevented verification of this characteristic of the model. On the other hand, the threshold criterion of Yokoyama (1988) for the evolution of the cumulative VT seismic

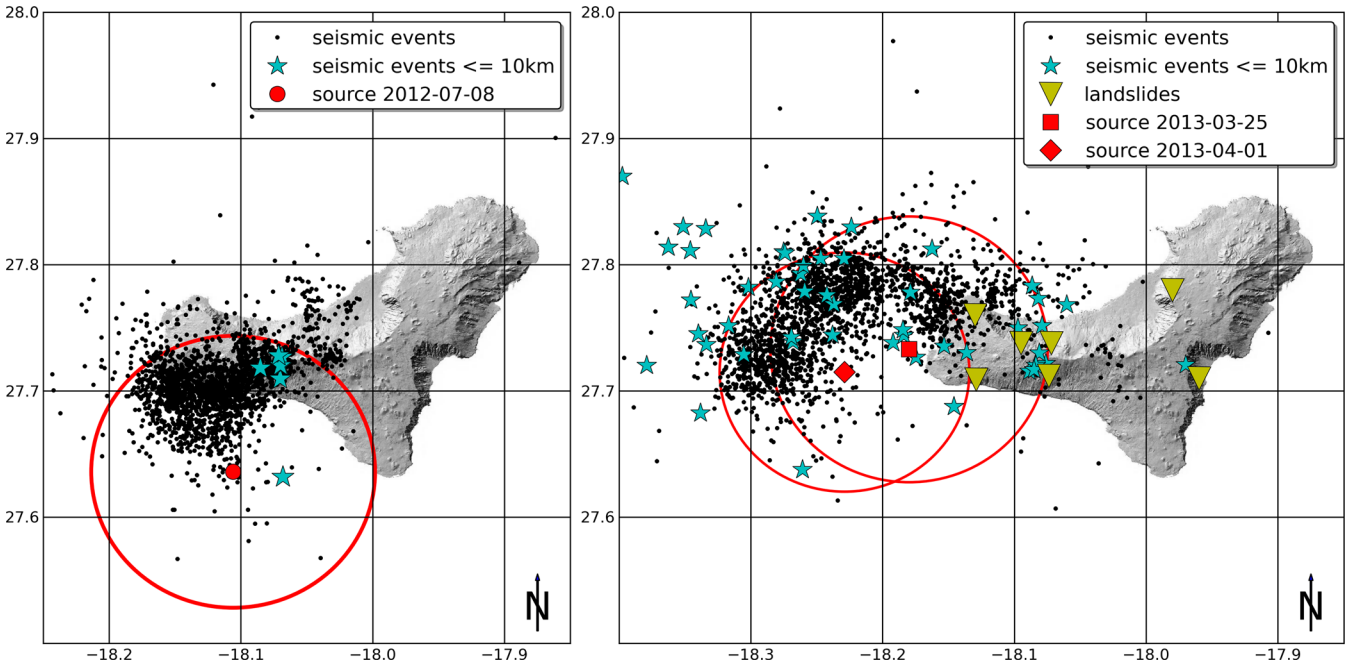

Figure 10. Evolution of seismicity in 2012 June–July and 2013 March–April. In the first period most hypocentres were located under the island, defining a sector for the 'injection' cone with its apex defined by a pressure source centre calculated from Mogi models. In 2013 March–April, several sources acted simultaneously, and the superficial earthquakes and landslides were concentrated in the proximities of the circumferences (landslide data from the El Pinar de El Hierro municipality).

energy proved to be a powerful tool, rather insensitive to the seismic network insufficiencies, for the temporal forecasting of the eruption, and thus for the management of the unrest situation.

The results of this analysis indicates that a large volume of magma has accumulated under the El Hierro island and that, as a result, various magma injection processes have occurred, at least one of them reaching the subaquatic crustal surface and causing an eruption. The magma injection episodes evidenced the unlikeliness of a direct rise of magma from the primary source to the surface, and revealed a stepwise magma migration process controlled by the distribution of the maximum differential stresses induced by each of the newly emplaced magma pressure sources, reactivating pre-existing zones of weakness and fractures or inducing new fracturing. New injections may be issued from either, the primary or the secondary magma storage centres, a configuration that is consistent with the model of Stroncik *et al.* (2009). Such linked episodes (as the initial pressure source would not be necessarily exhausted by the magma migrations), identified as distinct period of unrest, may be separated by considerable intervals of time. In addition, they confirm the argument that magma injection processes do not necessarily result in an imminent eruption (Gudmundsson 2000, 2002; Gudmundsson & Brenner 2001, 2004; De la Cruz-Reyna & Yokoyama 2011).

A major advantage of these simple forecast models is that they only require data of the temporal and spatial evolution of seismicity and deformation as it becomes available, as they do not require large computing facilities and they offer an almost real-time capability to provide decision makers with realistic scenarios and forecasts 24–48 hr in advance. More complex models usually require to be fed with, frequently unknown or assumed parameters, and may require intricate calculations and large computing capabilities.

On the other hand, some consequences of these models' simplicity may be questioned, particularly on the reliability of the simple Mogi model (Masterlark 2007) when dealing with the evaluation of the size and pressure of the source. Some objections to its application arise from the source dimension to source depth ratio approximation. Both, experience and theoretical approaches indicate that in most cases the simple Mogi model renders satisfactory results even when the implicit hypothesis of such ratio being negligible is not fulfilled. For example, Dvorak & Dzurisin (1997), and Widiwijayanti *et al.* (2005) apply this method to the study of shallow magma systems with good results. According to Lisowski (2006) lacking other data to guide a decision, the preferred model is the simplest one that fits the data within the expected error. To validate the application of the Mogi model to the study of the magma injection episodes at El Hierro, we have recalculated the inversions of the simple Mogi model using the McTigue (1987) finite spherical magma body model, and the results become only significantly different when the radius of the pressure source exceeds about one half of the source depth, an unlikely configuration in a basaltic system. In all other cases the difference between these models is less than the observational errors, as shown in Fig. 11, where ε is the source dimension to source depth ratio.

Another important question on the validity of the injection models is the apparent discrepancy between the depths calculated for the pressure centres obtained from the Mogi models and the distribution of earthquake depths. To explain this, it is important to consider that the hypocentre location is subject to a variety of difficulties, such as the size of the island making it difficult to locate earthquakes outside the seismic network, and an inadequate vertical distribution model of the seismic wave velocity, that may generate artificial voids in the vertical distribution of hypocentres.

We consider that the information provided by these models has proved useful for the decision makers to plan mitigation actions such as modification and refinement of the emergency plans, closing vulnerable infrastructures such as roads and tunnels, and

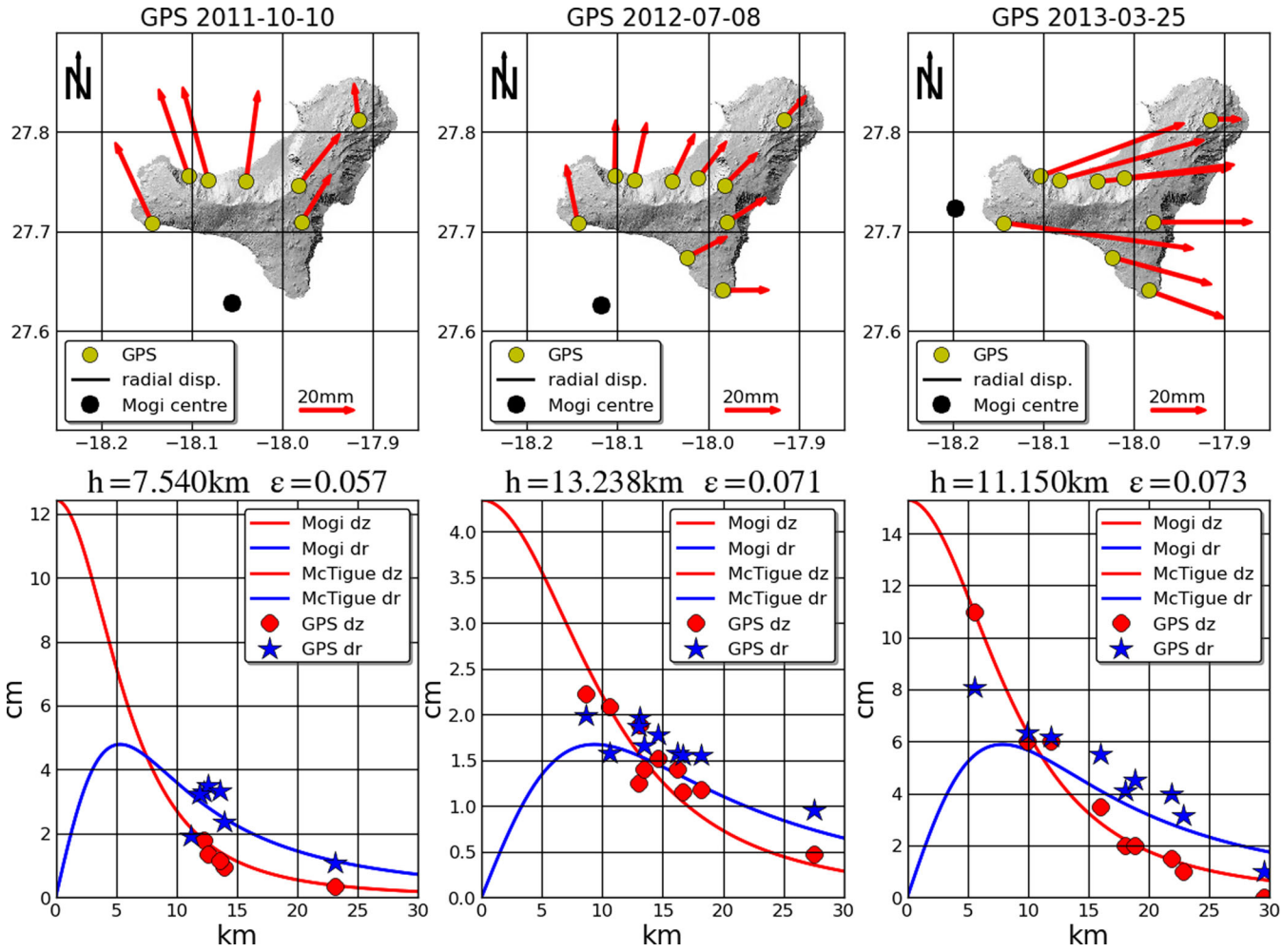

Figure 11. Comparative analysis of the simple Mogi models (Mogi 1958) and the finite spherical magma body models of McTigue (1987) used in this work. In the figure three different magma injection process (2011 October, 2012 June–July and 2013 March–April) are shown. ε is the source dimension to source depth ratio.

the evacuation of population in the proximities of the zones of possible landslides. The eruption of 2011 October, and the distribution of shallow earthquakes and the landslides that occurred in the episode of 2013 March–April constitute data-based validation of this methodology.

We may conclude that the models used here demonstrated their value as a tool for the management of the volcanic and seismic crises at El Hierro Island, and that it has a high potential of application in other cases of volcanic unrest, providing stakeholders with information about the nature of the ongoing process, as well as decision factors in almost real time (in less than 24 hr), as a crisis develops. Understanding the basic features of the physical process causing the unrest should be a first step in any crisis situation.

ACKNOWLEDGEMENTS

This research has been funded by the projects from the CSIC (2011-30E070), MINECO (CGL2011-28682-C02-01) and the bilateral UNAM (Mexico) - CSIC (Spain) program. The seismic and geodetic data used in this research were provided by the IGN, CSIC and UCA networks in the framework of the CSIC–IGN scientific collaboration and advice agreement (2006–2012). Additional data were obtained from the graphics on the public web pages of the IGN. All IGN data are © Instituto Geográfico Nacional. We are indebted to the Excmo. Cabildo Insular de El Hierro, and to its three municipalities (Valverde, El Pinar de El Hierro and Frontera) for their help installing and maintaining the instruments. We are also grateful to the Mayor's Office of El Pinar de El Hierro, and to the Mayor Juan Miguel Padrón, and to Jesús Pérez and Magaly González, for their help and support during the whole period of unrest at El Hierro. Last but not least, we wish to thank all of the people living on El Hierro for their encouragement and understanding of our scientific work.

REFERENCES

Ancochea, E., Hernán, F., Cendrero, A., Cantagrel, J.M., Fúster, J.M., Ibarrola, E. & Coello, J., 1994. Constructive and destructive episodes in the building of a young Oceanic Island, La Palma, Canary Islands, and genesis of the Caldera de Taburiente, *J. Volc. Geotherm. Res.,* **60**(3–4), 243–262.

Bell, A.F., Naylor, M., Heap, M.J. & Main, I.G., 2011. Forecasting volcanic eruptions and other material failure phenomena: an evaluation of the failure forecast method, *Geophys. Res. Lett.,* **38,** L15304, doi:10.1029/2011GL048155.

Berrocoso, M., Prates, G., Fernández-Ros, A. & García, A., 2012. Normal vector analysis from GNSS-GPS data applied to Deception volcano surface deformation, *Geophys. J. Int.,* **190,** 1562–1570.

Blanco-Montenegro, I., Nicolosi, I., Pignatelli, A. & Chiappini, M., 2008. Magnetic imaging of the feeding system of oceanic volcanic islands: El Hierro (Canary Islands), *Geophys. J. Int.,* **173**(1), 339–350.

Bosshard, E. & Macfarlane, D., 1970. Crustal structure of the western Canary Islands from seismic refraction and gravity data, *J. geophys. Res.-Sol. Earth.,* **75**(26), 4901–4918.

Carbó, A., Muñoz Martín, A., Llanes, P. & Álvarez, J. EEZ Working Group, 2003. Gravity analysis offshore the Canary Islands from a systematic survey, *Mar. geophys. Res.,* **24**(1–2), 113–127.

Carracedo, J., 1994. The Canary Islands: an example of structural control on the growth of large oceanic-island volcanoes, *J. Volc. Geotherm. Res.,* **60**(3–4), 225–241.

Carracedo, J.C., Day, S.J., Guillou, H. & Pérez-Torrado, F.J., 1999. Giant Quaternary landslides in the evolution of La Palma and El Hierro, Canary Islands, *J. Volc. Geotherm. Res.,* **94,** 169–190.

Carracedo, J.C., Rodríguez-Badiola, E.R., Guillou, H., de la Nuez, J. & Pérez-Torrado, F.J., 2001. Geology and volcanology of La Palma and El Hierro, Western Canaries, *Estu. Geol.,* **57**(5–6), 175–273.

Carracedo, J.C., Pérez-Torrado, F., Rodríguez-González, A., Soler, V., Fernández-Turiel, J.L., Troll, V.R. & Wiesmaier, S., 2012. The 2011 submarine volcanic eruption in El Hierro (Canary Islands), *Geol. Today,* **28**(2), 53–58.

Catalán, M. & Martín Davila, J., 2003. A magnetic anomaly study offshore the Canary Archipelago, *Mar. geophys. Res.,* **24,** 129–148.

Dach, R., Hugentobler, U., Fridez, P. & Meindl, M., 2007. *Bernese GPS Software Version 5.0. Tech. Rep.,* 612 p., Astronomical Institute, University of Bern.

Day, S., Carracedo, J. & Guillou, H., 1997. Age and geometry of an aborted rift flank collapse: the San Andres fault system, El Hierro, Canary Islands, *Geol. Mag.,* **134,** 523–537.

De la Cruz-Reyna, S. & Reyes-Dávila, G.A., 2001. A model to describe precursory material-failure phenomena: applications to short-term forecasting at Colima volcano, Mexico, *Bull. Volcanol.,* **63,** 297–308.

De la Cruz-Reyna, S. & Yokoyama, I., 2011. A geophysical characterization of monogenetic volcanism, *Geofis. Int.,* **50,** 465–484.

De la Cruz-Reyna, S., Yokoyama, I., Martinez-Bringas, A. & Ramos, E., 2008. Precursory seismicity of the 1994 eruption of Popocatepetl Volcano, Central Mexico, *Bull. Volcanol.,* **70**(6), 753–767.

Dvorak, J.J. & Dzurisin, D., 1997. Volcano geodesy: the search for magma reservoirs and the formation of eruptive vents, *Rev. Geophys.,* **35**(3), 343–384.

Dzurisin, D., 2006. *Volcano Deformation: New Geodetic Monitoring Techniques,* Springer.

Gee, M., Masson, D., Watts, A. & Mitchell, N., 2001a. Offshore continuation of volcanic rift zones, El Hierro, Canary Islands, *J. Volc. Geotherm. Res.,* **105**(1–2), 107–119.

Gee, M.J., Watts, A.B., Masson, D.G. & Mitchell, N.C., 2001b. Landslides and the evolution of El Hierro in the Canary Islands, *Mar. Geol.,* **177**(3–4), 271–293.

González, P.J. *et al.*, 2013. Magma storage and migration associated with the 2011-2012 El Hierro eruption: implications for crustal magmatic systems at oceanic island volcanoes, *J. geophys. Res.-Sol. Earth,* **118,** 1–17.

Gorbatikov, A., Montesinos, F., Arnoso, J. & Stepanova, M., 2010. El Hierro Island Model-Canary-On a basis of joint interpretation of microseismic sounding and gravity inversions, in *Proceedings of the European Association of Geoscientists & Engineers 4th International Conference & Exhibition, no. P211,* pp.1–5, European Association of Geoscientist & Engineers, Saint Petersburg, Russia.

Gudmundsson, A., 2000. Dynamics of volcanic systems in Iceland: example of tectonism and volcanism at juxtaposed hot spot and mid-ocean ridge systems, *Annu. Rev. Earth planet. Sci.,* **28**(1), 107–140.

Gudmundsson, A., 2002. Emplacement and arrest of sheets and dykes in central volcanoes, *J. Volc. Geotherm. Res.,* **116**(3–4), 279–298.

Gudmundsson, A. & Brenner, S.L., 2001. How hydrofractures become arrested, *Terra Nova,* **13**(6), 456–462.

Gudmundsson, A. & Brenner, S., 2004. Local stresses, dyke arrest and surface deformation in volcanic edifices and rift zones, *Ann. Geophys.-Italy,* **47**(4), 1433–1454.

Guillou, H., Carracedo, J., Pérez Torrado, F. & Rodríguez Badiola, E., 1996. K-Ar ages and magnetic stratigraphy of a hotspot-induced, fast grown oceanic island: El Hierro, Canary Islands, *J. Volc. Geotherm. Res.,* **73**(1–2), 141–155.

Hernández-Pacheco, A., 1982. Sobre una posible erupción en 1793 en la isla de El Hierro (Canarias), *Estu. Geol.,* **38**(1–2), 15–26.

Ibáñez, J.M., De Angelis, S., Díaz-Moreno, A., Hernández, P., Alguacil, G., Posadas, A. & Pérez, N., 2012. Insights into the 2011-2012 submarine eruption off the coast of El Hierro (Canary Islands, Spain) from statistical analyses of earthquake activity, *Geophys. J. Int.,* **191**(2), 659–670.

Kalman, R.E., 1960. A new approach to linear filtering and prediction problems, *J. Basic Eng.-T. Asme.,* **82**(1), 35–45.

Kilburn, C.R., 2003. Multiscale fracturing as a key to forecasting volcanic eruptions, *J. Volc. Geotherm. Res.,* **125**(3–4), 271–289.

Kilburn, C., 2012. Precursory deformation and fracture before brittle rock failure and potential application to volcanic unrest, *J. geophys. Res.-Sol. Earth,* **117,** B02211, doi:10.1029/2011JB008703.

Lisowski, M., 2006. Analytical volcano deformation source models, in *Volcano Deformation,* pp. 279–304, ed. Dzurisin, D., Springer.

López, C. *et al.*, 2012. Monitoring the volcanic unrest of El Hierro (Canary Islands) before the onset of the 2011–2012 submarine eruption, *Geophys. Res. Lett.,* **39,** L13303, doi:10.1029/2012GL051846.

Martí, J. *et al.*, 2013. Causes and mechanisms of El Hierro submarine eruption (2011-2012) (Canary Islands), *J. geophys. Res.-Sol. Earth,* **118**(3), 823–839.

Masson, D., Watts, A., Gee, M., Urgeles, R., Mitchell, N., Bas, T.L. & Canals, M., 2002. Slope failures on the flanks of the western Canary Islands, *Earth-Sci. Rev.,* **57**(1–2), 1–35.

Masterlark, T., 2007. Magma intrusion and deformation predictions: sensitivities to the Mogi assumptions, *J. geophys. Res.-Sol. Earth,* **112**(B6), B06419, doi:10.1029/2006JB004860.

McTigue, D., 1987. Elastic stress and deformation near a finite spherical magma body: resolution of the point source paradox, *J. geophys. Res.-Sol. Earth,* **92**(B12), 12 931–12 940.

Mitchell, N.C., Masson, D.G., Watts, A.B., Gee, M.J. & Urgeles, R., 2002. The morphology of the submarine flanks of volcanic ocean islands: a comparative study of the Canary and Hawaiian hotspot islands, *J. Volc. Geotherm. Res.,* **115**(1–2), 83–107.

Mogi, K., 1958. Relations between the eruptions of various volcanoes and the deformations of the ground surfaces around them, *B. Earthq. Res. Inst. Univ. Tokio,* **36,** 99–134.

Montesinos, F., Arnoso, J. & Vieira, R., 2005. Using a genetic algorithm for 3-D inversion of gravity data in Fuerteventura (Canary Islands), *Int. J. Earth Sci.,* **94,** 301–316.

Montesinos, F., Arnoso, J., Benavent, M. & Vieira, R., 2006. The crustal structure of El Hierro (Canary Islands) from 3-D gravity inversion, *J. Volc. Geotherm. Res.,* **150**(1–3), 283–299.

Ortiz, R., Moreno, H., García, A., Fuentealba, G., Astiz, M., Peña, P., Sánchez, N. & Tárraga, M., 2003. Villarrica volcano (Chile): characteristics of the volcanic tremor and forecasting of small explosions by means of a material failure method, *J. Volc. Geotherm. Res.,* **128**(1), 247–259.

Pérez, N.M. *et al.*, 2012. Precursory diffuse CO_2 and H_2S emission signatures of the 2011–2012 El Hierro submarine eruption, Canary Islands, *Geophys. Res. Lett.,* **39**(16), L16311, doi:10.1029/2012GL052410.

Prates, G., Berrocoso, M., Fernández-Ros, A. & García, A., 2013a. Enhancement of sub-daily positioning solutions for surface deformation monitoring at Deception volcano (South Shetland Islands, Antarctica), *Bull. Volcanol.,* **75,** 1–10.

Prates, G., García, A., Fernández-Ros, A., Marrero, J.M., Ortiz, R. & Berrocoso, M., 2013b. Enhancement of sub-daily positioning solutions for surface deformation surveillance at El Hierro volcano (Canary Islands, Spain), *Bull. Volcanol.,* **75**(6), 1–9.

Press, W.H., Teukolsky, S.A., Vetterling, W.T. & Flannery, B.P., 2007. Simulated annealing methods, in *Numerical Recipes 3rd Edition: The Art of Scientific Computing,* p. 1195, Cambridge Univ. Press.

Sezawa, K., 1931. The plastic-elastic deformation of a semi-infinite solid body due to an internal force, *B. Earthq. Res. Inst. Univ. Tokio,* **9,** 398–406.

Stroncik, N., Klügel, A. & Hansteen, T., 2009. The magmatic plumbing system beneath El Hierro (Canary Islands): constraints from phenocrysts and naturally quenched basaltic glasses in submarine rocks, *Contrib. Mineral. Petr.,* **157,** 593–607.

Tárraga, M., Carniel, R., Ortiz, R. & García, A., 2008. Chapter 13, the failure forecast method: review and application for the real-time detection of precursory patterns at reawakening volcanoes, *Dev. Volcanol.,* **10,** 447–469.

Voight, B., 1988. A method for prediction of volcanic eruptions, *Nature,* **332,** 125–130.

Voight, B. & Cornelius, R.R., 1991. Prospects for eruption prediction in near real-time, *Nature,* **350,** 695–698.

Watts, A.B., 1994. Crustal structure, gravity anomalies and flexure of lithosphere in the vicinity of the Canary Islands, *Geophys. J. Int.,* **119**(2), 648–666.

Widiwijayanti, C., Clarke, A., Elsworth, D. & Voight, B., 2005. Geodetic constraints on the shallow magma system at Soufrière Hills Volcano, Montserrat, *Geophys. Res. Lett.,* **32**(11), L11309, doi:10.1029/2005GL022846.

Yokoyama, I., 1988. Seismic energy releases from volcanoes, *Bull. Volcanol.,* **50,** 1–13.